

Plasmonic polaron in self-intercalated 1T-TiS₂

Byoung Ki Choi^{1,2†*}, Woojin Choi^{3†}, Zhiyu Tao^{4,5†}, Ji-Eun Lee^{1,6,7}, Sae Hee Ryu^{1,8}, Seungrok Mun³, Hyobeom Lee³, Kyoungree Park³, Seha Lee³, Hayoon Im⁹, Yong Zhong^{1,10,11}, Hyejin Ryu⁶, Min Jae Kim⁹, Sue Hyeon Hwang⁹, Xuetao Zhu^{4,5}, Jiandong Guo^{4,5}, Jong Mok Ok⁹, Jaekwang Lee⁹, Haeyong Kang⁹, Sungkyun Park⁹, Jonathan D. Denlinger¹, Heung-Sik Kim^{3,12}, Aaron Bostwick¹, Zhi-Xun Shen^{10,11}, Choongyu Hwang^{9*}, Sung-Kwan Mo^{1*}, and Jinwoong Hwang^{3*}

¹Advanced Light Source, Lawrence Berkeley National Laboratory, Berkeley, CA, USA.

²Technological Convergence Center, Korea Institute of Science and Technology, Seoul, Korea.

³Department of Physics and Institute of Quantum Convergence Technology, Kangwon National University, Chuncheon, Korea.

⁴Beijing National Laboratory for Condensed Matter Physics and Institute of Physics, Chinese Academy of Sciences, Beijing, China.

⁵School of Physical Sciences, University of Chinese Academy of Sciences, Beijing, China.

⁶Center for Semiconductor Technology, Korea Institute of Science and Technology, Seoul, Korea.

⁷Max Planck POSTECH Center for Complex Phase Materials, Pohang University of Science and Technology, Pohang 37673, Korea.

⁸Research Center for Beamline, Korea Basic Science Institute (KBSI), Daejeon, Korea.

⁹Department of Physics, Pusan National University, Busan, Korea.

¹⁰Geballe Laboratory for Advanced Materials, Department of Physics and Applied Physics, Stanford University, Stanford, CA, USA.

¹¹Stanford Institute for Materials and Energy Sciences, SLAC National Accelerator Laboratory, Menlo Park, CA, USA.

¹²Department of Energy Engineering, Korea Institute of Energy Technology, Naju-si, Korea.

† equal contribution

* Corresponding authors: bkchoi@kist.re.kr, SKMo@lbl.gov, ckhwang@pusan.ac.kr, jwhwang@kangwon.ac.kr

KEYWORDS: 1T-TiS₂, Electron-plasmon coupling, Plasmonic polaron, ARPES, EELS, DFT

Abstract

Electron-boson coupling is central to a comprehensive understanding of the diverse physical phenomena emerging from many-body interactions. Yet less attention has been paid to how plasmons, collective bosonic modes of electron density oscillation, interact with conduction electrons and how external parameters can tune this interaction. Here, we present a clear display of composite quasiparticles stemming from electron-plasmon coupling, known as the plasmonic polaron, in self-intercalated 1T-TiS₂, by using angle-resolved photoemission spectroscopy (ARPES), high-resolution electron energy loss spectroscopy (HR-EELS) and first-principles calculations. The single particle spectral function exhibits a distinctive plasmon-loss satellite with the same characteristic energy scale determined by HR-EELS measurements. The bosonic energy scale of plasmonic polaron is tunable by controlling charge carrier density and temperature, distinguishing itself from conventional polarons arising from electron-phonon interactions. Furthermore, we find that the dielectric screening strongly affects the formation of the plasmonic polaron states. Our findings provide direct spectroscopic evidence of plasmonic polarons and establish self-intercalated layered materials as a promising platform for studying, controlling, and harnessing plasmonic interactions in quantum materials.

The interaction of electrons with collective bosonic modes in solids is of practical and fundamental interest in condensed matter physics. This interaction not only affects the transport properties of actual devices but also induces novel quantum phenomena. A prominent example is the formation of polarons, composite quasiparticles of electrons dressed in phonon clouds due to the strong electron-phonon interaction¹. Polarons lead to significantly enhanced quasiparticle mass that modifies charge carrier transport properties, and play a critical role in superconducting and many-body phenomena in high- T_c cuprates^{2,3}, manganites⁴, two-dimensional (2D) electron gases in heterostructures⁵, transition metal dichalcogenides^{6,7}, and superconducting monolayer FeSe⁸. Other notable examples include electron-magnon interactions in ferromagnetic metals⁹ and electron interactions with antiferromagnetic spin fluctuations in iron-based superconductors¹⁰.

Less studied electron-boson coupling in solids is the interaction between electrons and plasmons, quasiparticles of collective charge density oscillations. The electron-plasmon coupling can produce composite quasiparticles known as plasmarons or plasmonic polarons, characterized by distinctive plasmon-loss satellites in the energy spectrum^{1,11}, analogous to polarons from electron-phonon interaction^{12,13}. Plasmonic polarons exhibit unique properties distinct from conventional phonon-induced polarons, which may offer advantages in specific applications. Notably, plasmonic polarons generally have higher characteristic energies and greater tunability than phononic polarons¹¹. Since plasmons are excited with a characteristic frequency (ω_{plasmon}) related to the carrier density (n), plasmon energy can be effectively modulated by altering the charge carrier density^{13,14} and temperature¹⁵⁻¹⁷. Furthermore, electron-plasmon coupling can significantly impact the low-energy properties of materials, such as enhancing quasiparticle mass and limiting charge carrier mobilities^{2,18}.

Despite the important role of electron-plasmon coupling in determining the electronic properties of solids, the plasmonic polaron has been scarcely investigated in real materials. The scarcity is primarily due to the relatively weak electron-plasmon coupling strength¹⁸ and the challenge of achieving sufficiently high doping levels to drive a material system into a well-defined plasmonic regime while maintaining stoichiometry. To date, only a limited number of studies have reported this phenomenon, primarily focusing on heavily electron-doped oxide semiconductors and 2D materials all in their thin film forms^{12,13,19}, often involving external treatments such as post-annealing, surface irradiation^{5,12}, or extrinsic surface carrier doping^{14,19}. Consequently, open questions still remain about whether there is a way to achieve an optimal charge carrier density to realize well-defined plasmonic polaron signatures in bulk materials without external treatments and how these signatures could be distinguished from those of other bosonic excitation modes.

In this paper, we report a direct observation of plasmonic polarons formed by electron-plasmon coupling in self-intercalated $1T$ -TiS₂, using angle-resolved photoemission spectroscopy (ARPES) and high-resolution electron energy loss spectroscopy (HR-EELS) measurements. Our experimental results reveal that bulk $1T$ -TiS₂ is a highly electron-doped semiconductor with a band gap of ~ 0.5 eV due to self-intercalated Ti atoms, which serve as a charge reservoir between $1T$ -TiS₂ layers. The most pronounced feature in an ARPES band structure is a satellite band at ~ 0.2 eV below the conduction band minimum, typically observed in a polaronic system due to “shake-off” excitations in the photoemission process²⁰. HR-EELS clearly distinguishes between phonon and plasmon excitation energies and uncovers that the bulk plasmon excitation corresponds to the polaronic energy obtained in ARPES. First-principle many-body calculations, including the calculated plasmon self-energy, successfully reproduce the satellite band, confirming the formation of plasmonic polarons in self-intercalated $1T$ -TiS₂. Furthermore, we find that the energy of the satellites

in self-intercalated 1T-TiS₂ is tunable by varying the charge carrier density, in agreement with the expectation within the plasmonic polaron picture, and that the modification of the band structure and dielectric environment by temperature strongly affects the formation of the plasmonic polaron. Our findings demonstrate that plasmonic polarons can be formed intrinsically in bulk materials via interstitial adatoms, providing a versatile material platform enabling a systematic study of the plasmonic polaron state.

Results and Discussion

Atomic and electronic structures of 1T-TiS₂ and Ti self-intercalated 1T-TiS₂

Figure 1a illustrates the crystal structure of the layered octahedral 1T-TiS₂, which crystallizes in a CdI₂-type layered structure (*P-3m1*) with a hexagonal Ti sublayer sandwiched between two S sublayers. The three sublayers constitute a single layer of 1T-TiS₂, weakly bonded to adjacent layers by van der Waals forces. It is generally known that foreign atoms can easily enter in the van der Waals gaps in transition metal dichalcogenides (TMDCs)^{21,22}. In the case of 1T-TiS₂, the self-intercalation of Ti atoms has been directly observed, and theoretical analysis suggests that excess Ti is energetically more favorable than S vacancies²³. The extra atoms are randomly distributed between 1T-TiS₂ layers²³ and our Raman spectrum further supports the presence of intercalated Ti atoms, indicated by a broad shoulder peak (Sh) on the high-energy side of the A_{1g} peak (Figure S1)^{22,24}. Energy-dispersive X-ray spectroscopy (EDX) analysis (Figure S2) confirms the non-stoichiometric composition of TiS₂, which would give a chemical formula Ti_{1.089}S₂, assuming Ti intercalation. To account for the Ti intercalation in our calculation, we have adopted Hubbard *U* correction to Ti 3*d* orbitals and added excess electrons in 1T-TiS₂. Figure 1b presents a density functional theory (DFT) calculation for self-intercalated 1T-TiS₂, which accurately reproduces the ARPES data from the as-cleaved self-intercalated sample shown in Figure 1c. Using orbital-projected calculations via Wannier functions, we find that the

valence band maximum (VBM) at the Γ point is primarily composed of S $3p$ orbitals, while the conduction band minimum (CBM) at the M point is dominated by Ti $3d$ orbitals (Figure S3).

While the overall ARPES band features are well matched with the DFT+ U calculations (green dashed lines in Figure 1c), the calculated band structures do not replicate the additional satellite feature observed ~ 0.24 eV below the Fermi energy (E_F) at the M point. This satellite band displays not only the well-defined “peak-dip-hump” structure but also a broad tail concentrated at higher binding energies at the M point (Figure 1d). The satellite feature exhibits momentum dependence, as evidenced by ARPES constant-energy maps (CEMs) (Figure S4). This satellite spectral feature resembles well-known polaronic states reported in previous ARPES studies^{12,13,19,25,26}. The entire conduction band is scattered by a particular bosonic mode to higher binding energies, while the original band shape is preserved due to shake-off excitations of the bosonic mode during the photoemission process²⁰ (Figure 4b). Therefore, new spectral weight in the ARPES intensity map (Figure 1d) emerges due to these excitations below the quasiparticle band, separated by bosonic-excitation energy ($\hbar\Omega$). These characteristic features (the QP pocket at M and its satellite) were consistently observed across multiple cleaved samples and at different locations on each sample. While the self-intercalated Ti atoms are microscopically distributed at random (Ref. 23), our ARPES measurements—which average over a macroscopic beam spot (~ 50 - 100 μm)—reveal a highly uniform and reproducible electronic structure. This indicates that the self-intercalation is macroscopically homogeneous.

Plasmonic polaron in the self-intercalated 1T-TiS₂

In order to identify the bosonic mode coupled with electron, we have conducted low-energy excitation measurements using HR-EELS. Figure 2a shows a boson momentum (q)-resolved HR-EELS spectrum taken along the Γ -M direction at 35 K. The HR-EELS measurements reveal two characteristic collective excitations in self-intercalated 1T-TiS₂. A low-energy excitation mode within below ~ 50 meV originates from the lattice vibrations (phonon). It is well matched with the energy scale of the calculated phonon modes for self-intercalated 1T-TiS₂ (Figure S5). Another excited bosonic mode appears in the HR-EELS spectrum at ~ 200 meV. This high-energy mode is distinct from the phonon dispersion, with peak intensity strong only near the Γ and rapidly diminishing as the momentum increases (Figure S6). This characteristic feature is well described by the Landau damping in plasmon dispersion, where the plasmon decays into single particle electron-hole pair excitations^{27,28}. In addition, the non-zero plasmon loss energy at $q = 0.0 \text{ \AA}^{-1}$ indicates that the experimentally obtained bosonic mode at ~ 200 meV originates from the bulk plasmon. Other possible collective modes, such as exciton or impurity states, can be reasonably ruled out due to the transient nature of exciton and momentum dependence of the observed satellites^{29,30}. Given the similar energy scale of the ARPES satellite band at the M-point (Figure 1d), we conclude that the bosonic excitation coupled with electrons in self-intercalated 1T-TiS₂ is indeed the bulk plasmon rather than a phonon.

One of the key distinctions between conventional polarons, originating from the electron-phonon coupling, and plasmonic polarons is the charge carrier density dependence of their characteristic excitation energy. While the characteristic energy of phonon modes (e.g. Fröhlich polaron) remains independent of charge carrier density^{11,12,20}, the characteristic energy of the plasmonic polarons can be tuned by the carrier concentration^{11,12,14}. To delineate the nature of the bosonic mode by tuning the charge carrier density further, we deposited Rb atoms on the surface of the as-cleaved self-

intercalated 1*T*-TiS₂ at 20 K³¹. The overall spectral shift to higher binding energy reflects an increased Fermi energy due to electron doping (Figures. 2**b-e** and Figure S7,8). More importantly, the characteristic energy ($\hbar\Omega$) determined by separation between the quasiparticle (QP) and satellite peaks at the M point increases with rising charge carrier density, from 197 ± 0.8 meV ($n = 1.37 \times 10^{21}$ cm⁻³) to 214 ± 1.2 meV ($n = 4.43 \times 10^{21}$ cm⁻³), as shown in Figure 2**f**. The increased satellite energy supports the formation of plasmonic polarons and highlights the possibility of manipulating these composite particles by tuning the charge carrier density.

The formation of the plasmonic polaron is further supported by the density functional perturbation theory (DFPT). Figure 2**g** shows the calculated spectral intensity, modified by the calculated plasmon self-energy using the cumulant expansion method (Figure S9). Our DFPT calculation accurately reproduces the spectral weight of the plasmon satellite state observed in the ARPES results (Figure 2**h**), clearly demonstrating the formation of plasmonic polaron in self-intercalated 1*T*-TiS₂. We note that the spectral intensity in Figure 2**h** only shows the first-order satellite feature, with no higher-order satellites observed, unlike other polaronic features reported in the literature^{8,12-14,26}. Based on the energy distribution curve (EDC) profile of ARPES data taken at M point (Figure 1**f**), the first-order satellite has ~8 times less intensity compared to the quasiparticle peak. Assuming that the second-order satellite weight is reduced by a similar factor, its intensity would be at the background level^{12,13,19} (Figure S10).

Temperature-dependent plasmonic dynamics in self-intercalated 1*T*-TiS₂

Further insights into plasmonic polaron states can be gained by examining the temperature dependence of ARPES satellite features, as plasmon energy has a subtle yet clear temperature dependence¹⁵⁻¹⁷. Until now, the temperature-dependence study in plasmonic polaron systems has been considered challenging, as these states are typically induced by light irradiation, dosing of the adatoms on the surface, or ferromagnetic transition^{12,13,19,26}, which are not sustainable at high temperatures. In contrast, the self-intercalated 1T-TiS₂, with its robust interstitial Ti atoms, is well-suited for investigating temperature-dependent plasmonic states.

Figure 3a presents the temperature-dependent HR-EELS spectra for self-intercalated 1T-TiS₂ taken at $q = 0.0 \text{ \AA}^{-1}$. The obtained HR-EELS spectra exhibit three features with increasing temperature: (i) a gradual shift of the bulk plasmon resonance peak towards lower loss energy, (ii) a reduction in the plasmon peak intensity, and (iii) an increase in the full width at half maximum (FWHM). These behaviors correspond well to plasmon damping due to increased electron-electron and electron-phonon scatterings at elevated temperatures^{16,27,32}. The plasmon damping effects are also captured in the plasmonic polaronic state in ARPES results. Figure 3b shows the temperature-dependent ARPES spectra taken at the M point, where the plasmonic polaron state emerges (Figure 1d). With increasing temperature, EDCs clearly show a reduction in spectral weight of QP peaks along with suppression of the plasmon satellite peak (Figure 3b and S11). To characterize the temperature-dependent plasmon damping, we plot the FWHMs of both HR-EELS and ARPES spectra in Figure 3c. The FWHMs of the plasmon state in both spectra increase dramatically ($\sim 50 \text{ meV}$), while QP FWHM increases more moderately ($\sim 12 \text{ meV}$). As temperature rises, plasmonic polarons become rapidly unstable compared to the QP peak due to plasmon damping from enhanced lattice vibrations and thermal excitations, leading to the dissolution of polaronic states at high temperatures^{16,27,32}. As a result, the features

associated with plasmonic polarons weaken, and FWHM increases with reduced QP intensity due to increased inelastic scattering, consistent with HR-EELS observations. We further notice that both QP and satellites peaks in ARPES spectra shift to higher binding energies with increasing temperature, but the satellite peak moves less, reducing the separation between the QP and satellite peaks (Figure 3b (inset) and S12).

In Figure 3d, the bosonic energies extracted from ARPES (red points) and HR-EELS (green points) both decrease with increasing temperatures. To investigate the temperature dependence of electron-plasmon coupling, we extracted the charge carrier density (n) and the effective mass (m^*) of the electron pocket at the M point from ARPES data. Our analysis reveals a gradual increase in n and a decrease in m^* with rising temperature (Figure S13). Considering the relation for bulk plasmon energy, $\hbar\Omega \propto \sqrt{n/\epsilon m^*}$, the temperature dependent behavior of $\sqrt{n/m^*}$ contrasts sharply with the observed reduction in plasmon energy at higher temperatures (Figures 3d and 4a). This discrepancy suggests that the dielectric constant (ϵ) must increase with temperature to reconcile the observed trends in n and m^* , indicating that ϵ plays a critical role in modulating plasmon energy as a function of temperature (Figure 4a). To extract $1/\epsilon$, we have used the plasmon energy relation of $\hbar\Omega \propto \sqrt{n/\epsilon m^*}$, where the plasmon energy ($\hbar\Omega$) and $\sqrt{n/m^*}$ were extracted from ARPES results (Figs. 3d, S12 and S14). As ϵ can be influenced by changes in n and crystal structure^{33,34}, the observed increase in n partially contributes to the enhancement of ϵ at elevated temperatures. The minor discrepancies between plasmon energies measured by ARPES and HR-EELS (Fig. 3d) can be attributed to the different mechanisms inherent to these techniques^{32,35-37}.

Additionally, temperature-dependent in-plane tensile stress of 1T-TiS₂ further contributes to the overall temperature dependence of plasmon energies. Temperature-

dependent ARPES data show an unexpected band shift at the Γ point, where the S-induced hole band shifts to higher binding energy with increasing temperature. This band shift is well reproduced by DFT calculations under an in-plane tensile stress of $\sim 1.3\%$, consistent with Raman spectroscopy measurements²² (Figures S15 and S16). These findings suggest that observed tensile stress is an additional factor influencing the temperature evolution of plasmonic energy. Therefore, a comprehensive understanding of plasmonic polarons requires the combined use of ARPES, HR-EELS, and theoretical calculations.

It is fascinating to notice that similar satellite features in ARPES spectra have been discussed in connection with the enhancement of superconductivity, e.g., at the interface of single-layer FeSe and SrTiO₃^{8,38} and Cr-intercalated ZrTe₂³⁹. While BCS theory may be extended to a general bosonic field including plasmon¹, it is not yet clear whether plasmonic polaron may play a similar role as the phononic polarons in creating and enhancing superconductivity. It would be interesting to see whether it is possible to find similar satellite features through the intercalation of charge-donating atoms in the van der Waals gap of superconducting TMDCs such as NbSe₂^{40,41}, and how the superconductivity is affected when plasmonic polarons are formed in these systems.

In summary, our combined investigation with ARPES, HR-EELS, and DFT on the exotic bosonic coupling in self-intercalated 1T-TiS₂ unambiguously confirms the presence of plasmonic polarons. This result establishes self-intercalated material as a promising platform to utilize the plasmonic polaron with a highly tunable electronic structure that can be modified by carrier density and temperature. Our study demonstrates that TMDCs are ideal materials for the creation, study, and control of plasmonic polarons in bulk, owing to their propensity to incorporate additional transition metal atoms into the van der Waals gap between layers⁴²⁻⁴⁴. Moreover, its layered structure and intrinsic plasmonic nature make

self-intercalated 1T-TiS₂ advantageous for constructing van der Waals heterostructures, which is promising in exploiting plasmonic physics, such as realizing high-temperature superconductors through hybrid phonon-plasmon coupling and opening new opportunities for plasmonic applications.

Methods

Sample and ARPES measurement

The self-intercalated 1T-TiS₂ single crystals were purchased from HQ Graphene. The EDX measurements were performed at the Korea Institute of Science and Technology (KIST) to determine the ratio of atomic weights. ARPES data were taken at Beamlines 10.0.1 and 4.0.3, Advanced Light Source, Lawrence Berkeley National Laboratory, using Scienta R4000 and R8000 analyzers, respectively. The base pressure was better than 4×10^{-11} Torr. The photon energy was set at 52 eV for *p*-polarizations with energy and angular resolution of 18–25 meV and 0.1°, respectively. To achieve high-quality ARPES data of self-intercalated TiS₂, the samples were cleaved at low temperatures (~20 K). Rubidium (Rb) deposition was carried out by *in-situ* evaporation of Rb on the sample surfaces using a commercial SAES getter source mounted in the analysis chamber.

HR-EELS measurements

The 1T-TiS₂ single crystals were also examined with an HR-EELS system equipped with an Ibach-type ELS5000 monochromator from LK technologies and an Scienta R4000 analyzer⁴⁵

HR-EELS measurements were performed at temperatures ranging from 35 K to 291 K with a primary electron beam energy of 110 eV.

Density Functional Theory Calculations

All DFT and DFPT calculations for 1T-TiS₂ (space group $P\bar{3}m1$) were performed using the Quantum ESPRESSO⁴⁶ package. We adopted the Hubbard corrections (DFT+ U) for hopping mechanism of intercalation with an effective onsite Coulomb parameter $U = 3.25$ eV for Ti (3d). The generalized gradient approximation (GGA) of Perdew, Burke and Ernzerhof for solids (PBEsol) exchange-correlation functionals and norm-conserving pseudopotentials were used. We employed a plane wave kinetic energy cutoff of 50 Ry (680 eV), kinetic energy cutoff for charge density and potential for norm-conserving pseudopotential of 500 Ry, and $12 \times 12 \times 12$ Monkhorst-Pack mesh to sample the Brillouin zone. Estimated self-consistent field accuracy is equal to 1×10^{-12} Ry. The phonon dispersions were obtained with a $4 \times 4 \times 4$ supercell. To illustrate the real space orbital and orbital projected bands, we used Wannier function disentanglement with Wannier90⁴⁷. We used cumulant expansion function in EPW code⁴⁸ to obtain spectral functions with electron-phonon and electron-plasmon self-energy. The retarded electron self-energy is driven by Raleigh-Schrödinger perturbation theory:

$$\int \frac{dq}{\Omega_{\text{BZ}}} \sum_{m\nu} |g_{mn}^{\nu}(\mathbf{k}, \mathbf{q})|^2 \left[\frac{n(\omega_{q\nu}) + f(\epsilon_{\mathbf{m}\mathbf{k}+\mathbf{q}})}{\epsilon_{\mathbf{n}\mathbf{k}} - \epsilon_{\mathbf{m}\mathbf{k}+\mathbf{q}} - \omega_{q\nu} - i\eta} + \frac{n(\omega_{q\nu}) + 1 - f(\epsilon_{\mathbf{m}\mathbf{k}+\mathbf{q}})}{\epsilon_{\mathbf{n}\mathbf{k}} - \epsilon_{\mathbf{m}\mathbf{k}+\mathbf{q}} + \omega_{q\nu} - i\eta} \right].$$

Here, $\epsilon_{\mathbf{m}\mathbf{k}+\mathbf{q}}$ is electron energy, $n(\omega_{q\nu})$ is the Bose occupation factors, $f(\epsilon_{\mathbf{m}\mathbf{k}+\mathbf{q}})$ is Fermi-Dirac occupation factors, η is infinitesimal, $\omega_{q\nu}$ is plasmon/phonon frequency. The $g_{mn}^{\nu}(\mathbf{k}, \mathbf{q})$ represents matrix elements between the initial state $\psi_{\mathbf{n}\mathbf{k}}$ and the final state $\psi_{\mathbf{m}\mathbf{k}+\mathbf{q}}$ for electron-phonon and electron-plasmon coupling⁴⁹ given by

$$g_{mn}^v(k, q) = \langle \Psi_{mk+q} | \partial_{qv} V | \Psi_{nk} \rangle, \text{ and } g_{mn}^v(k, q) = \left[\frac{\epsilon_0 \Omega}{e^2 \hbar} \frac{\partial \epsilon(q, \omega)}{\partial \omega} \right]_{\omega_q}^{-1/2} \frac{1}{|q|} \langle \Psi_{mk+q} | e^{iq \cdot r} | \Psi_{nk} \rangle$$

, respectively, with $\partial_{qv} V$ the derivative of the self-consistent potential associated with a phonon of wavevector q , v branch index, Ω the volume of one unit cell.

Acknowledgements

This research used resources of the Advanced Light Source, which is a DOE Office of Science User Facility under contract no. DE-AC02-05CH11231. BKC and JEL were supported in part by an ALS Collaborative Postdoctoral Fellowship. The work at the SIMES/Stanford is supported by the U.S. Department of Energy, Office of Basic Energy Sciences, Division of Materials Sciences and Engineering, under Contract No. DE-AC02-76SF00515. J.H. acknowledges financial support from the National Research Foundation of Korea (NRF) grant funded by the Korean government (MSIT) (RS-2023-00280346), the GRDC (Global Research Development Center) Cooperative Hub Program through the NRF funded by the Ministry of Science and ICT (MIST) (RS-2023-00258359), and Semiconductor R&D Support Project through the Gangwon Technopark (GWTP) funded by Gangwon Province (No. GWTP 2023-027). C.H. acknowledges financial support from NRF grant funded by the Ministry of Science and ICT (RS-2025-25453111, RS-2023-00221154, RS-2022-NR068223), the KBSI (NFEC) grant funded by the Ministry of Education (RS-2024-0043534, RS-2021-NF000587), and PNU-RENovation(2023-2024). H. R. and BKC acknowledges financial support from the KIST Institutional Program (2E33581, 2V10511). H. R. acknowledges financial support from the NRF (2020R1A5A1016518) and NST (GTL24041-000) grants by the MSIT.

Author contributions

B.K.C., J.W.H., C.H. and S.-K.M. initiated and conceived the research. J.W.H., B.K.C. and W.J.C. performed the ARPES measurements with the help from S.H.R., J.-E.L., H.B.L., K.R.P., S.H.L., J.D.D, H.J.R and Y.Z. and under the supervision of S.-K.M., A.B., Z.-X.S. and C.H. J.W.H. and B.K.C. analyzed the ARPES data. S.R.M., H.-S.K., J.L., and B.K.C. performed DFT calculations and theoretical analyses. Z.T. performed the HR-EELS measurements under the supervision of X.Z. and J.G., and S.H.H., M.J.K., J.M.O., S.P., H.K., and C.H. analyzed the HR-EELS data. B.K.C., W.J.C., J.W.H., C.H., Y.Z. and S.-K.M. wrote the manuscript with the help from all authors. All authors contributed to the scientific discussion.

Competing interests

The authors declare no competing interests.

Data availability

The data that support the plots within this paper and other findings of this study are available from Jinwoong Hwang (jwhwang@kangwon.ac.kr), who will respond to requests for data upon reasonable request.

References

- 1 Alexandrov, A. S. & Devreese, J. T. *Advances in polaron physics*. Vol. 159 (Springer, 2010).

- 2 Lanzara, A. *et al.* Evidence for ubiquitous strong electron–phonon coupling in high-
temperature superconductors. *Nature* **412**, 510-514 (2001).
- 3 Shen, K. *et al.* Missing Quasiparticles and the Chemical Potential Puzzle in the Doping
Evolution of the Cuprate Superconductors. *Phys. Rev. Lett.* **93**, 267002 (2004).
- 4 Mannella, N. *et al.* Nodal quasiparticle in pseudogapped colossal magnetoresistive
manganites. *Nature* **438**, 474-478 (2005).
- 5 Meevasana, W. *et al.* Creation and control of a two-dimensional electron liquid at the
bare SrTiO₃ surface. *Nat. Mater.* **10**, 114-118 (2011).
- 6 Kang, M. *et al.* Holstein polaron in a valley-degenerate two-dimensional semiconductor.
Nat. Mater. **17**, 676-680 (2018).
- 7 Emeis, C., Mahatha, S. K., Rohlf, S., Rossnagel, K. & Caruso, F. Plasmonic polarons
induced by alkali-atom deposition in hafnium disulfide 1T-HfS₂. *Phys. Rev. B* **108**,
155149 (2023).
- 8 Lee, J. *et al.* Interfacial mode coupling as the origin of the enhancement of T_C in FeSe
films on SrTiO₃. *Nature* **515**, 245-248 (2014).
- 9 Raquet, B., Viret, M., Sondergard, E., Cespedes, O. & Mamy, R. Electron-magnon
scattering and magnetic resistivity in 3d ferromagnets. *Phys. Rev. B* **66**, 024433 (2002).
- 10 Scalapino, D. The cuprate pairing mechanism. *Science* **284**, 1282-1283 (1999).
- 11 Caruso, F., Verdi, C. & Giustino, F. Many-body calculations of plasmon and phonon
satellites in angle-resolved photoelectron spectra using the cumulant expansion
approach. *Handbook of Materials Modeling: Methods: Theory and Modeling*, 341-365
(2020).
- 12 Ma, X. *et al.* Formation of plasmonic polarons in highly electron-doped anatase TiO₂.
Nano Lett. **21**, 430-436 (2020).
- 13 Riley, J. M. *et al.* Crossover from lattice to plasmonic polarons of a spin-polarised
electron gas in ferromagnetic EuO. *Nat. Commun.* **9**, 2305 (2018).
- 14 Ulstrup, S. *et al.* Observation of interlayer plasmon polaron in graphene/WS₂
heterostructures. *Nat. Commun.* **15**, 3845 (2024).
- 15 Yeshchenko, O., Bondarchuk, I., Gurin, V., Dmitruk, I. & Kotko, A. Temperature
dependence of the surface plasmon resonance in gold nanoparticles. *Surf. Sci.* **608**, 275-
281 (2013).
- 16 Rocca, M., Moresco, F. & Valbusa, U. Temperature dependence of surface plasmons
on Ag (001). *Phys. Rev. B* **45**, 1399 (1992).
- 17 Gervais, F., Servoin, J.-L., Baratoff, A., Bednorz, J. G. & Binnig, G. Temperature
dependence of plasmons in Nb-doped SrTiO₃. *Phys. Rev. B* **47**, 8187 (1993).
- 18 Lundqvist, B. & Samathiyakanit, V. Single-particle spectrum of the degenerate electron
gas. *Phys. kondens. Materie* **9**, 231-235 (1969).
- 19 Caruso, F. *et al.* Two-dimensional plasmonic polarons in *n*-doped monolayer MoS₂.
Phys. Rev. B **103**, 205152 (2021).
- 20 Hüfner, S. *Very high resolution photoelectron spectroscopy*. Vol. 715 (Springer
Science & Business Media, 2007).
- 21 Suga, S. *et al.* Momentum microscopy of the layered semiconductor TiS₂ and Ni
intercalated Ni_{1/3}TiS₂. *New J. Phys.* **17**, 083010 (2015).
- 22 Dużyńska, A. *et al.* Temperature-induced phonon behavior in titanium disulfide (TiS₂)
nanosheets. *J. Raman Spectrosc.* **50**, 1114-1119 (2019).
- 23 Wang, H. *et al.* Semimetal or semiconductor: the nature of high intrinsic electrical
conductivity in TiS₂. *J. Phys. Chem. Lett.* **10**, 6996-7001 (2019).
- 24 Klipstein, P., Bagnall, A., Liang, W., Marseglia, E. & Friend, R. Stoichiometry
dependence of the transport properties of TiS₂. *J. Phys. C: Solid State Phys.* **14**, 4067
(1981).

- 25 Chen, C., Avila, J., Frantzeskakis, E., Levy, A. & Asensio, M. C. Observation of a two-dimensional liquid of Fröhlich polarons at the bare SrTiO₃ surface. *Nat. Commun.* **6**, 8585 (2015).
- 26 Moser, S. *et al.* Tunable polaronic conduction in anatase TiO₂. *Phys. Rev. Lett.* **110**, 196403 (2013).
- 27 Segui, S., Gervasoni, J. L. & Arista, N. R. Plasmon damping in the free-electron gas model of solids. *Nucl. Instrum. Methods Phys. Res. B* **408**, 217-222 (2017).
- 28 Lin, Z. *et al.* Dramatic Plasmon Response to the Charge-Density-Wave Gap Development in 1T-TiSe₂. *Phys. Rev. Lett.* **129**, 187601 (2022).
- 29 Mori, R. *et al.* Spin-polarized spatially indirect excitons in a topological insulator. *Nature* **614**, 249-255 (2023).
- 30 Kastl, C. *et al.* Effects of defects on band structure and excitons in WS₂ revealed by nanoscale photoemission spectroscopy. *ACS Nano* **13**, 1284-1291 (2019).
- 31 Choi, B. K. *et al.* Visualizing orbital content of electronic bands in anisotropic 2D semiconducting ReSe₂. *ACS Nano* **14**, 7880-7891 (2020).
- 32 Rocca, M. Low-energy EELS investigation of surface electronic excitations on metals. *Surf. Sci. Rep.* **22**, 1-71 (1995).
- 33 Cockayne, E. Influence of oxygen vacancies on the dielectric properties of hafnia: First-principles calculations. *Phys. Rev. B* **75**, 094103 (2007).
- 34 Abdelkadir, A. A. *et al.* Analysis of the temperature dependent optical properties of V_{1-x}W_xO₂ thin films. *Thin Solid Films* **772**, 139805 (2023).
- 35 Li, F. & Sawatzky, G. A. Electron phonon coupling versus photoelectron energy loss at the origin of replica bands in photoemission of FeSe on SrTiO₃. *Phys. Rev. Lett.* **120**, 237001 (2018).
- 36 Bostwick, A. *et al.* Observation of plasmarons in quasi-freestanding doped graphene. *Science* **328**, 999-1002 (2010).
- 37 Walter, A. L. *et al.* Effective screening and the plasmaron bands in graphene. *Phys. Rev. B* **84**, 085410 (2011).
- 38 Zhang, C. *et al.* Ubiquitous strong electron–phonon coupling at the interface of FeSe/SrTiO₃. *Nat. Commun.* **8**, 14468 (2017).
- 39 Zhang, B. *et al.* Electronic structures of Cr-intercalated ZrTe₂ revealed by angle-resolved photoemission spectroscopy. *J. Phys. Chem. C* **124**, 16561-16567 (2020).
- 40 Lu, J. *et al.* Evidence for two-dimensional Ising superconductivity in gated MoS₂. *Science* **350**, 1353-1357 (2015).
- 41 Xi, X. *et al.* Ising pairing in superconducting NbSe₂ atomic layers. *Nat. Phys.* **12**, 139-143 (2016).
- 42 Zhao, X. *et al.* Engineering covalently bonded 2D layered materials by self-intercalation. *Nature* **581**, 171-177 (2020).
- 43 Zhang, H. *et al.* Tailored Ising superconductivity in intercalated bulk NbSe₂. *Nat. Phys* **18**, 1425-1430 (2022).
- 44 Ahn, Y. *et al.* Converting the Bulk Transition Metal Dichalcogenides Crystal into Stacked Monolayers via Ethylenediamine Intercalation. *Nano Lett.* **23**, 9733-9739 (2023).
- 45 Zhu, X. *et al.* High resolution electron energy loss spectroscopy with two-dimensional energy and momentum mapping. *Rev. Sci. Instrum.* **86**, 803902 (2015).
- 46 Giannozzi, P. *et al.* QUANTUM ESPRESSO: a modular and open-source software project for quantum simulations of materials. *J. Condens. Matter Phys.* **21**, 395502 (2009).
- 47 Mostofi, A. A. *et al.* wannier90: A tool for obtaining maximally-localised Wannier functions. *Comput. Phys. Commun.* **178**, 685-699 (2008).

- 48 Noffsinger, J. *et al.* EPW: A program for calculating the electron–phonon coupling using maximally localized Wannier functions. *Comput. Phys. Commun.* **181**, 2140–2148 (2010).
- 49 Caruso, F. & Giustino, F. Theory of electron-plasmon coupling in semiconductors. *Phys. Rev. B* **94**, 115208 (2016).

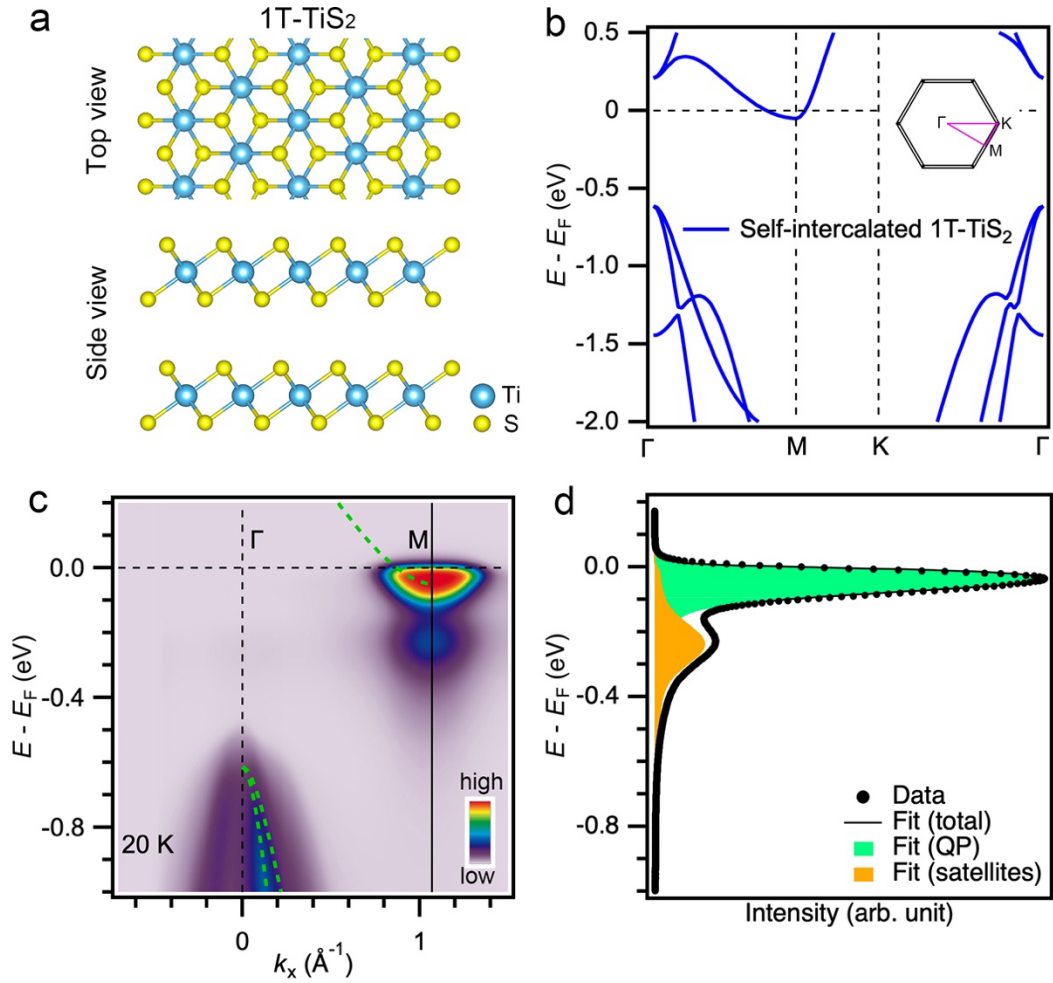


Figure 1 Atomic and electronic structures of 1T-TiS₂ and Ti self-intercalated 1T-TiS₂. **a**, Top- and side-view schematics of TiS₂ with 1T structure. The sky-blue and yellow balls represent the Ti and S atoms, respectively. **b**, DFT calculated electronic structures of self-intercalated TiS₂ with 1T structure. Hubbard U correction to Ti 3d orbitals and added excess electrons are adopted in 1T-TiS₂ to mimic the electronic structure of the self-intercalated 1T-TiS₂. The amount of doped electron is one electron per 8 unit-cells. (Inset: The Brillouin zone of 1T-TiS₂ with high-symmetry points.) **c**, ARPES spectra of the as-cleaved self-intercalated TiS₂ (Ti_{1.089}S₂) along the Γ -M direction for Ti-intercalated TiS₂ with the p -polarization. Calculated bands are overlapped with green dashed line. **d**, Energy distribution curve (EDC) taken at $k_x = 1.07 \text{ \AA}^{-1}$ (M point). Green and orange areas indicate quasiparticle peak and its satellite peak, respectively.

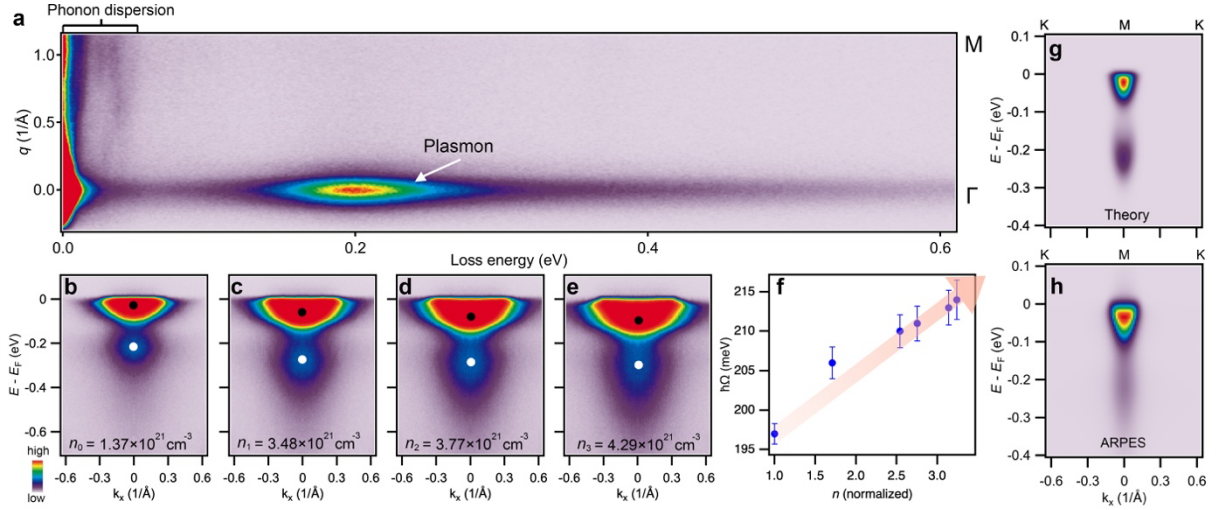


Figure 2 Plasmonic polaron in the self-intercalated 1T-TiS₂. **a**, Boson momentum-resolved HR-EELS of the self-intercalated 1T-TiS₂ at 35 K. q indicates boson momentum transfer. **b-e**, ARPES intensity maps of self-intercalated 1T-TiS₂ sample after additional electron doping via in-situ Rb deposition. **f**, The evolution of bosonic energy extracted from ARPES data (**b-e**) as a function of n . **g-h**, DFPT calculated spectral function and ARPES spectra along the K–M–K direction for self-intercalated 1T-TiS₂. The calculated spectral function is post-processed with Gaussian broadening and Fermi-Dirac statistic (Figure S7).

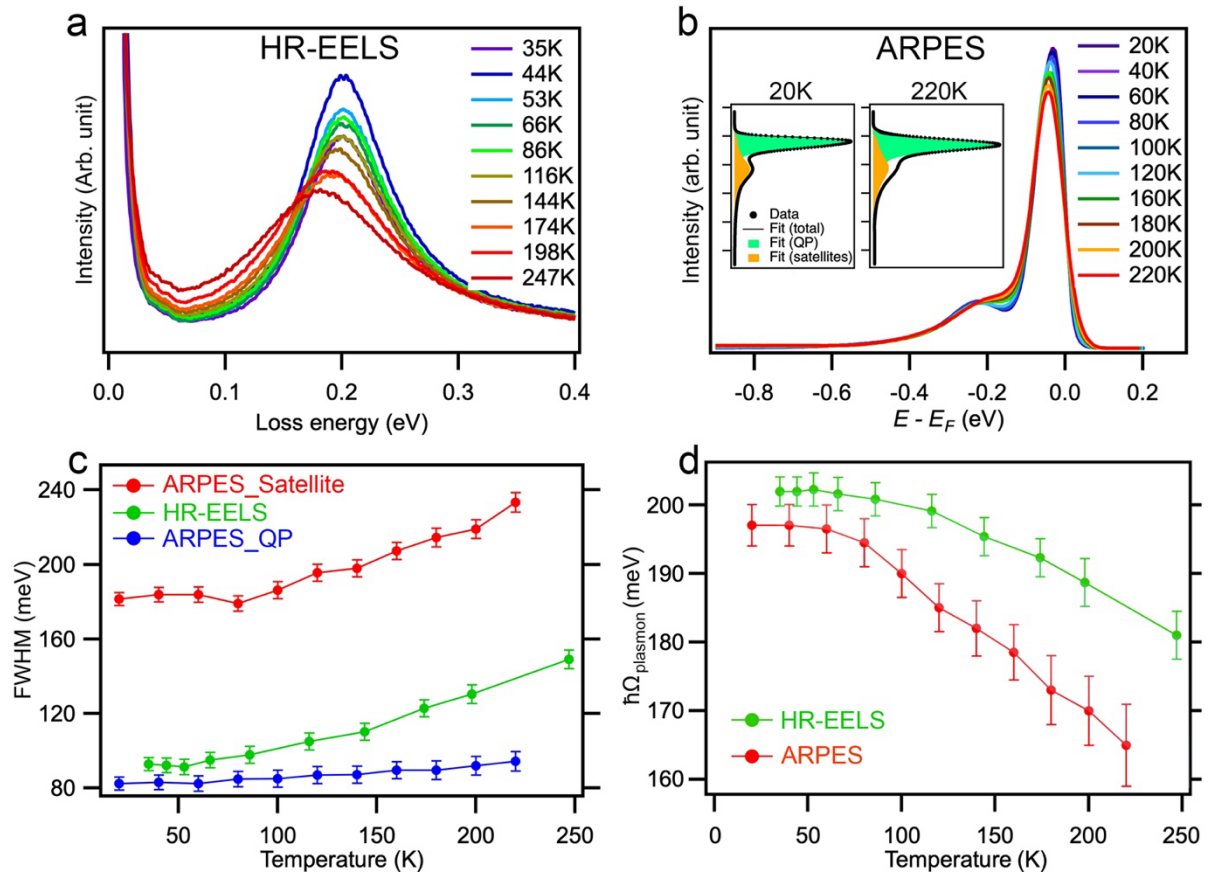


Figure 3 Temperature-dependent plasmonic dynamics in self-intercalated 1T-TiS₂. **a**, Temperature-dependent EDCs obtained from EELS at $q = 0.0 \text{ \AA}^{-1}$. **b**, Temperature-dependent EDCs obtained from ARPES at the M point. **c**, Temperature-dependent FWHMs obtained from satellite and QP peaks in ARPES (red and blue points) and HR-EELS (green points), respectively. **d**, Evolution of bosonic energy obtained from ARPES (red points) and HR-EELS (green points) as a function of temperature.

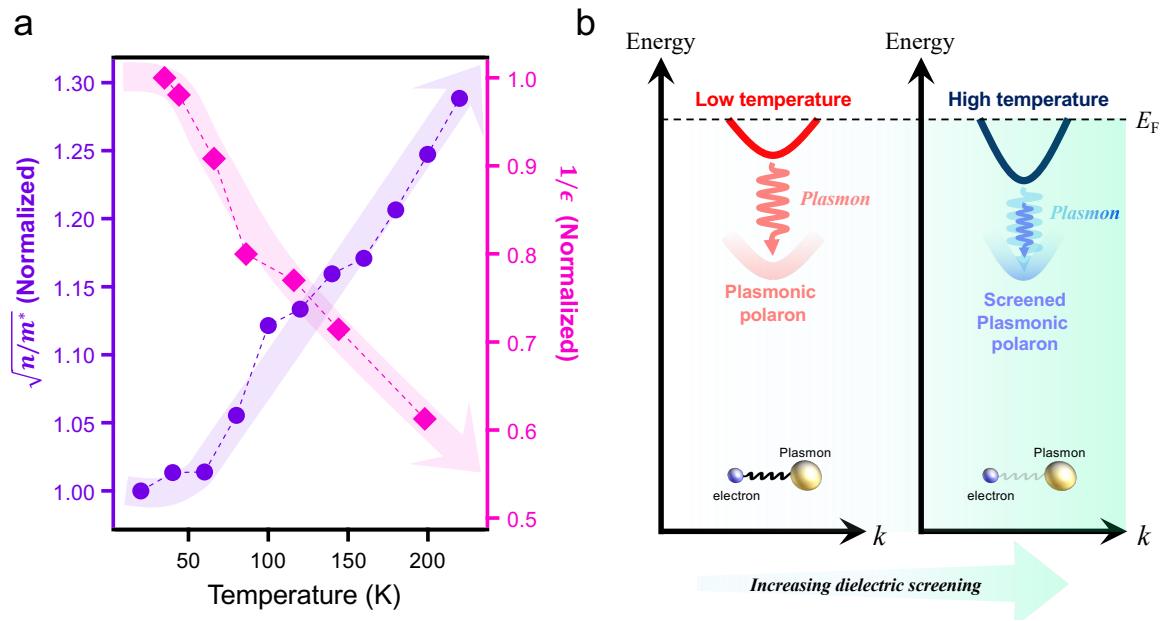


Figure 4 Temperature-dependent many-body characteristic of self-intercalated 1T-TiS₂.

a, Normalized values of $\sqrt{n/m^*}$ (purple circles) and $1/\epsilon$ (pink rhombus) as a function of temperature, respectively. The normalizations were based on the value of 20 K. **b**, Schematic illustrating the formation of the plasmonic polaron in self-intercalated 1T-TiS₂ at low and high temperatures. Light green background indicates the increase of the dielectric screening.